

# ***In situ* spectroscopic ellipsometry growth studies on the Al-doped ZnO films deposited by remote plasma-enhanced metalorganic chemical vapor deposition**

I. Volintiru,<sup>a)</sup> M. Creatore,<sup>b)</sup> and M. C. M. van de SandenDepartment of Applied Physics, Eindhoven University of Technology, P.O. Box 513,  
5600 MB Eindhoven, The Netherlands

(Received 9 August 2007; accepted 27 November 2007; published online 7 February 2008)

*In situ* spectroscopic ellipsometry (SE) was applied to study the pyramidlike and pillarlike growth of Al doped ZnO (AZO) films deposited by means of remote plasma-enhanced metalorganic chemical vapor deposition for transparent conductive oxide applications. Real time SE studies in the visible region allowed discerning between the two growth modes by addressing the time evolution of the bulk and surface roughness layer thickness. While the pillarlike mode is characterized by a constant growth rate, a slower rate in the initial stage (up to 150–200 nm film thickness), compared to the bulk, is observed for the growth of pyramidlike AZO films. The two modes differ also in terms of surface roughness development: a saturation behavior is observed for film thickness above 150–200 nm in the case of the pyramidlike films, while a slow linear increase with film thickness characterizes the pillarlike mode. By extending the SE analysis of the AZO films to the near infrared region, valuable information about the in grain properties could be extracted: excellent in grain mobility values, i.e., larger than 100 and 50 cm<sup>2</sup>/V s, are determined for the pyramidlike and pillarlike AZO layers, respectively. The comparison between the outcome of the *in situ* real time SE studies and the *ex situ* electrical and chemical characterization highlights the limitations in the electron transport occurring in both types of films and allows one to address routes toward further improvement in AZO conductivity. © 2008 American Institute of Physics.

[DOI: 10.1063/1.2837109]

## **I. INTRODUCTION**

Presently, zinc oxide (ZnO) is one of the most researched transparent conductive oxides (TCOs) as alternative to tin-doped indium oxide and fluorine-doped tin oxide for electrodes in solar cell and diode applications.<sup>1,2</sup> Its advantages are the high transparency in the visible part of the spectrum (>80%), the low resistivity ( $<5 \times 10^{-4} \Omega \text{ cm}$ ), the relatively high natural abundance of Zn, and low cost of the materials involved.<sup>3</sup> ZnO can be deposited using various techniques, the most widespread being (reactive) magnetron sputtering of ZnO and Zn targets,<sup>4</sup> pulsed layer deposition,<sup>5</sup> and metalorganic chemical vapor deposition (MOCVD).<sup>6,7</sup> By using plasma in combination with the MOCVD technique the process window is enlarged, e.g., the plasma-induced decomposition of the metalorganic precursors facilitates the use of lower deposition temperatures. Although plasma-enhanced MOCVD (PE-MOCVD) is not yet a widespread technique for ZnO deposition, its potential has already been demonstrated in a few studies.<sup>8</sup> Within our group, a remote PE-MOCVD technique has been used to deposit natively textured Al-doped ZnO (AZO) films, which have been successfully applied as front electrodes in *a*-Si solar cell applications.<sup>9</sup>

A recent observation and a serious challenge of ZnO deposition by MOCVD is the strong dependence of the elec-

trical properties on the film thickness.<sup>10</sup> This outcome was also observed in our PE-MOCVD process and a detailed study of the sheet resistance evolution during the growth of AZO was presented in previous work.<sup>11</sup> In Ref. 11 a set of *ex situ* electrical, morphological, and compositional diagnostic measurements was employed in order to identify the main causes for the sheet resistance gradient. Moreover, a tool to control the gradient and film growth mode was presented. Scanning electron microscopy (SEM) and atomic force microscopy (AFM) revealed a pyramidlike growth, with a distinctive grain development, under specific conditions (cf. type I in Table I), accompanying the large sheet resistance gradient (from 180  $\Omega/\square$  at 300 nm to 5.5  $\Omega/\square$  at 1.3  $\mu\text{m}$ ). The electron concentration (doping level) and film composition, determined by means of Hall and time-of-flight

TABLE I. The film properties for the type I (pyramidlike) and type II (pillarlike) AZO films;  $d_{\text{sp}}$  denotes the film thickness measured with the step profiler.

Parameter	ZnO:Al type I	ZnO:Al type II
$d_{\text{sp}}$ (nm)	940	820
rms (nm)	40	10
[Al] (%)	0.2	0.7
$R_s$ ( $\Omega/\square$ )	10	18
$N_e$ (cm <sup>-3</sup> ) <sup>a</sup>	$1.2 \times 10^{20}$	$1 \times 10^{20}$
$\mu$ (cm <sup>2</sup> /V s) <sup>a</sup>	12	5.3

<sup>a</sup>Measured on the aged films.<sup>a)</sup>Electronic mail: i.m.volintiru@tue.nl.<sup>b)</sup>Author to whom correspondence should be addressed. Electronic mail: m.creatore@tue.nl.

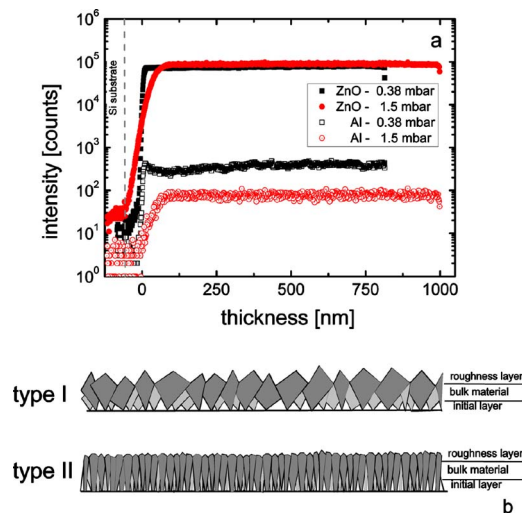


FIG. 1. (Color online) TOF-SIMS measurements (a) and qualitative growth model (b) of the type I (pyramidlike) and type II (pillarlike) AZO film growth (experimental conditions in Table I).

secondary ion mass spectrometry (TOF-SIMS) techniques, were found to be constant during growth. As a consequence, the strong sheet resistance gradient and the electron mobility evolution, determined by Hall, were related to the strong lateral grain size development. Note that the electrical measurements, i.e., four point probe and Hall, monitor both the in grain and intergrain electronic properties; therefore, no information on the in grain quality of the AZO films can be extracted solely from these measurements.

Due to the well developed grains (200–300 nm, as shown by SEM) and relatively high electron concentration ( $2 \times 10^{20} \text{ cm}^{-3}$ ), the final sheet resistance, i.e., for film thickness larger than 1200 nm, reaches a satisfactory level for solar cell applications.<sup>12</sup> Moreover, the films deposited are also rough ( $>4\%$  of the thickness) without any post-treatment, which is beneficial for light trapping within solar cells. Even though the pyramidlike growth mode is suitable for solar cells, it has two disadvantages: the sheet resistance gradient, already mentioned, and the poor nucleation, as indicated by TOF-SIMS analysis in Fig. 1(a), which shows the presence of an incubation layer of about 150 nm.

As shown in our previous article, the growth mode can be influenced by decreasing the working pressure, which promotes a transition from pyramidlike (type I) to pillarlike (type II) growth [Fig. 1(b)]. The latter is characterized by almost no resistivity gradient, accompanied by a limited grain and roughness development, and by a better initial nucleation (as indicated by TOF-SIMS). The downside of the type II AZO films, however, is the high sheet resistance ( $65 \text{ } \Omega/\square$  at 1125 nm), caused by the small grain size and low doping efficiency ( $\sim 20\%$  compared with  $96\%$  in the case of type I films).

The present article investigates further the two growth modes presented already in Ref. 11 by addressing two important issues:

- (1) In Ref. 11 the film growth was studied via a set of elaborate and often destructive *ex situ* measurements. Could the two growth modes of the AZO films be monitored

and, more important, “predicted,” *in situ* real time by means of a nonintrusive technique?

- (2) Besides the grain size, an important factor limiting the film sheet resistance can be the scattering at impurities inside the grains. As mentioned before, the electrical measurements monitor both the in grain and intergrain properties. In order to extract the in grain quality of the AZO films an optical technique, which can give information about the film properties at subgrain scale ( $<10 \text{ nm}$ ), is necessary.

A tool which can address both research questions is spectroscopic ellipsometry (SE). *Ex situ* SE has already been often applied to determine the optical constants and thickness of several deposited materials, including TCOs.<sup>13–15</sup> Up-to-now few groups have reported on the *in situ* and real time use of SE on the growth of different materials, such as Si,<sup>16,17</sup> titanium,<sup>18</sup>  $\text{TiO}_2$ ,<sup>19</sup> or GaN.<sup>20</sup> Related to ZnO, Losurdo *et al.*<sup>21</sup> reported *in situ* real time monitoring by SE of the changes in Zn- and O-polar ZnO surfaces upon interaction with H generated in a remote radio frequency plasma, while Groenen *et al.*<sup>22</sup> monitored the surface modification occurring during the etching process of ZnO by a remote Ar/ $\text{H}_2$  plasma. To our knowledge, the *in situ* and real time use of SE for the ZnO film growth is still relatively unexplored.<sup>23,24</sup>

In this article we describe the growth studies performed by *in situ* SE measurements on types I and II AZO films, deposited by remote PE-MOCVD. In Sec. II the ellipsometry model is presented and validated via comparison with the *ex situ* measurements previously addressed in Ref. 11. Section III is divided into two parts, providing answers to both research questions. In the first part the thickness and roughness evolution during film growth are determined from the optical model and used to identify the two growth modes. The second part is dedicated to the in grain electronic properties, which, in combination with the *ex situ* data presented in Ref. 11, give a reliable picture of the limiting electron transport processes in the AZO films.

## II. EXPERIMENTAL DETAILS AND DATA ANALYSIS

### A. Deposition setup and experimental conditions

AZO films were deposited using an expanding thermal plasma<sup>25</sup> fed by argon, generated in a high pressure (360 mbar) cascaded arc and expanding in a low pressure deposition chamber (0.3–1.5 mbar). The precursors for film deposition, i.e., diethylzinc (DEZ), oxygen, and trimethylaluminum (TMA), are injected downstream via injection rings. The typical conditions used for ZnO film deposition are listed in Table II. The substrates used for the experiments presented here are 400 nm thermal  $\text{SiO}_2$  on single side polished *c*-Si (for ellipsometry and electrical measurements) and Corning glass (for transmission measurements). Our results suggest that *c*-Si/ $\text{SiO}_2$  is indiscernible from the glass substrate, i.e., the AZO growth is similar on both types of substrates.

TABLE II. The deposition conditions used for the type I (pyramidlike) and type II (pillarlike) AZO films.

Deposition parameter	ZnO:Al type I	ZnO:Al type II
$\phi_{Ar}$ (sccm)	1000	1000
$I_{arc}$ (A)	50	50
$\phi_{O_2}$ (sccm)	100	100
$\phi_{DEZ}$ (g/h)	3.5	3.5
$\phi_{TMA}$ (g/h)	0.2	0.2
$p$ (mbar)	<b>1.5</b>	<b>0.38</b>
$T_{subs}$ (°C)	200	200

To acquire the  $(\Psi, \Delta)$  ellipsometric spectra on the AZO films grown on *c*-Si/SiO<sub>2</sub>, we used a Woollam M2000 spectroscopic ellipsometer in the 300–1700 nm wavelength range and the corresponding WVASE32 software to process the data. The *in situ* measurements were performed at an angle of 61°, set by the reactor geometry, with a time resolution of 12 s. For the *ex situ* SE measurements an angle of 75° was used.

## B. Spectroscopic ellipsometry analysis

Similar to the work of Groenen *et al.*,<sup>26</sup> a three-layer model, consisting of a semi-infinite Si substrate with a 400 nm-thick SiO<sub>2</sub> layer, a ZnO bulk, and a surface roughness layer, was chosen for the deposited films (Fig. 2). In order to simplify the ellipsometric analysis, a few assumptions were made, i.e., abrupt and smooth interfaces between different layers and isotropic optical constants, uniform in depth, for the film. These assumptions have been commonly used in literature for TCOs, although there have been also studies treating the inhomogeneity in depth of the TCOs (Ref. 27) and the anisotropy in ZnO.<sup>28</sup> The spectroscopic ellipsometry analysis was performed only on ZnO films with reasonably low roughness ( $<\lambda_{SE}/10$ ), such that extreme light depolarization could be avoided.

Tabulated values provided by the WVASE program were used for the optical constants of the semi-infinite silicon substrate at room temperature (for the *ex situ* measurements), as well as for the thermal 400 nm-SiO<sub>2</sub> layer on top. For the *in situ* measurements material files generated from the experimental data, collected on Si at 200 °C, were used as virtual substrate.

The most commonly used optical models in ultraviolet-visible (VIS) in literature for TCOs are Lorentz,<sup>29–31</sup> Cauchy,<sup>32</sup> and Sellmeier.<sup>33</sup> The latter two are simplified forms of the Lorentz representation and are suitable for any material in its transparency wavelength region.<sup>34</sup> More rarely applied are the Tauc–Lorentz<sup>14</sup> and Forouhi–Bloomer<sup>35</sup> mod-

els. For the free carrier absorption in the near infrared region (NIR), the Drude model is commonly employed for TCOs and metals, to analyze either the SE data or, when they are not available, the transmission data.<sup>36,37</sup> In this work we use a Cauchy–Drude model, the total dielectric function  $\epsilon = \epsilon_1 + i\epsilon_2$  being expressed as

$$\epsilon = \epsilon_{\text{Cauchy}} + \epsilon_{\text{Drude}}. \quad (1)$$

The Cauchy term  $\epsilon_{\text{Cauchy}}$  is used in the transparency range of the material, i.e., 400–1000 nm for the AZO films, and it is described by Eqs. (2a) and (2b),

$$n(\lambda) = A + \frac{B}{\lambda^2}, \quad (2a)$$

$$k(\lambda) = 0, \quad (2b)$$

where  $n$  and  $k$  are the refractive index and extinction coefficient, while  $A$  and  $B$  are the Cauchy parameters. The set of fitting parameters in the Cauchy model is  $(d_b, d_r, A, B)$ , where  $d_b$  and  $d_r$  are the bulk and the surface roughness thickness, respectively.

The optical constants  $(n, k)$  are related to the real and imaginary part of the dielectric constant  $(\epsilon_1, \epsilon_2)$  at each wavelength by Eqs. (3a) and (3b),

$$\epsilon_1 = n^2 - k^2, \quad (3a)$$

$$\epsilon_2 = 2nk \quad (3b)$$

The refractive index was determined at a film thickness of 200–250 nm for both types of AZO films and kept constant while modeling the *in situ* data. This thickness was chosen because it represents the “bulk” ZnO [cf. TOF-SIMS in Fig. 1(a)] and, at the same time, is characterized by reasonably low roughness ( $<10$  nm) so that light depolarization does not affect the modeling results, as earlier mentioned. The resulting values for the refractive index at 633 nm are 1.86 for type I and 1.92 for type II films. The value is higher for the type II films due to the compact, columnar structure growth, which leads to higher film density.<sup>11</sup>

The Drude model uses a single Lorentz oscillator with the center energy fixed to zero

$$\epsilon_{\text{Drude}}(E) = -\frac{A_D}{E^2 - i\Gamma_D E}, \quad (4)$$

where  $A_D$  and  $\Gamma_D$  are the oscillator amplitude and broadening, respectively. The set of fitted Drude parameters is  $(\epsilon_\infty, A_D, \Gamma_D)$ , expressed by

$$A_D = \epsilon_\infty \hbar^2 \omega_p^2, \quad (5a)$$

$$\Gamma_D = \hbar \gamma_D, \quad (5b)$$

where  $\epsilon_\infty$  represents the high-energy dielectric constant,<sup>38</sup>  $\hbar$  is the reduced Planck’s constant,  $\omega_p$  is the plasma frequency, and  $\gamma_D$  is the damping factor expressed in cm<sup>−1</sup>.

For better accuracy, the two models were applied separately in the corresponding wavelength regions. The optical constants obtained from the Cauchy and Drude representations were compared with the ones obtained from the point-

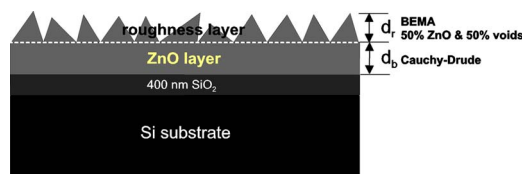


FIG. 2. (Color online) The optical model used to fit the ellipsometric data, consisting of a Si/SiO<sub>2</sub> substrate, a ZnO film, and a roughness layer.



by-point fits, i.e., using only the Kramer–Kronig relations, where the thickness was fixed from the Cauchy fit. Due to the assumptions in the two models, i.e.,  $k=0$  in the 400–1000 nm range (Cauchy) and  $k>0$  for  $\lambda>1000$  nm (Drude), the transition between the data points corresponding to the two models is not continuous. Therefore, in the transition region, a point by point fit was used.

From the Drude (free electron) theory<sup>39</sup> the electronic properties of the material can be deduced, i.e., the SE resistivity  $\rho_{\text{opt}}$ , the electron concentration  $N_{\text{opt}}$ , and the mobility  $\mu_{\text{opt}}$ , according to the formulas

$$\rho_{\text{opt}} (\Omega \text{ cm}) = \frac{\hbar}{e} \frac{\Gamma_D (\text{eV})}{\varepsilon_0 e A_D (\text{eV}^2)}, \quad (6a)$$

$$N_{\text{opt}} (\text{cm}^{-3}) = \frac{\varepsilon_0 m_e^* A_D (\text{eV}^2)}{\hbar^2}, \quad (6b)$$

$$\mu_{\text{opt}} \left( \frac{\text{cm}^2}{\text{V s}} \right) = \frac{\hbar}{m_e^* \Gamma_D (\text{eV})}, \quad (6c)$$

where  $m_e^*$  is the electron effective mass in the ZnO lattice and  $\varepsilon_0$  is the permittivity of free space. The errors in the optical resistivity, carrier concentration, and mobility have been determined from the Drude modeling of AZO films deposited under the same conditions (with similar properties). The modeling of the real time data also contains the error in mobility, i.e., for relatively small variations in thickness, the mobility can vary within the range used to estimate the errors.

The rough surface layer was modeled according to the Bruggeman effective medium approximation,<sup>40</sup> consisting of 50% bulk and 50% voids. This is in line with the work of various other groups on rough films.<sup>41</sup> In this model, the resulting refractive index of the top layer ( $n_{\text{top}}$ ) is considered to be a weighted average between the refractive index of the bulk material ( $n_{\text{bulk}}$ ) and that of the ambient ( $n_{\text{ambient}}$ ),

$$f_{\text{voids}} \frac{n_{\text{ambient}}^2 - n_{\text{top}}^2}{n_{\text{ambient}}^2 + 2n_{\text{top}}^2} + (1 - f_{\text{voids}}) \frac{n_{\text{bulk}}^2 - n_{\text{top}}^2}{n_{\text{bulk}}^2 + 2n_{\text{top}}^2} = 0, \quad (7)$$

where  $f_{\text{voids}}$  represents the void fraction ( $f_{\text{voids}}=0.5$ ) and  $n_{\text{ambient}}=1$  (air/vacuum).

### C. Validation of the SE model: Thickness and optical bulk properties

The ellipsometry models and their application wavelength ranges were chosen after analyzing the transmission spectra, for both types of films (see Fig. 3). Three distinct regions can be observed in these figures: the band gap absorption below 400 nm (region A), the transparency domain between 400 and 1000 nm (region B), and a decrease in transmission caused by free carrier absorption in the near infrared, i.e., above 1000 nm (region C). In region B the interference fringes are visible only for the columnar films, as a proof of their smooth surface morphology.

As a consequence of these observations we chose the Cauchy model in region B and Drude model in region C, while in region A we only performed a point by point fit.

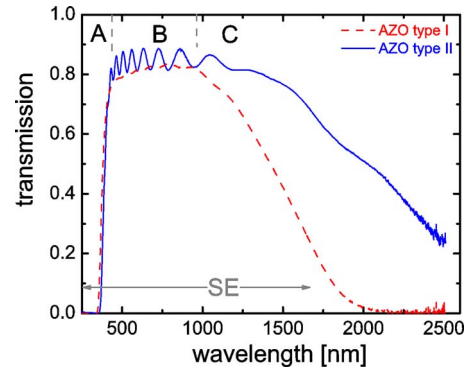


FIG. 3. (Color online) Typical transmission spectra of a 940 nm-type I (pyramidlike) and 820 nm-type II (pillarlike) deposited AZO films (experimental conditions in Table I).

Figure 4 shows a good agreement between the measured and fitted  $\Psi$  and  $\Delta$  curves, for thick films ( $>800$  nm). Poorer fits are obtained for rough films, which can be due to depolarization effects present at high roughness values,<sup>41</sup> but also to the errors involved in the interpretation of the roughness layer in the optical model.

As a next step we compared the film thickness given by ellipsometry ( $d_{\text{SE}}=d_b+d_r$ ) (Ref. 42) with the outcome of the step profiler measurements  $d_{\text{sp}}$ , which are found to agree within 10% error (Fig. 5). The agreement is good if we take into account the errors involved in the step profiler measurement, of  $\pm 30$  nm, and the error in the roughness layer thickness determined by SE, which depends on the void percentage assumed in the model. The biggest underestimation of the thickness by SE occurs, again, for the roughest samples.

Finally, we determined the optical constants from the Cauchy and Drude models and compared them with the values resulted from the point by point fitting procedure,<sup>43</sup> as shown in Fig. 6. To make the discussion complete, we used for comparison also an undoped ZnO (UZO) film, deposited under similar conditions as type II films, with the TMA flow set to zero. For this film a Cauchy layer in regions B and C was sufficient, due to the low carrier concentration

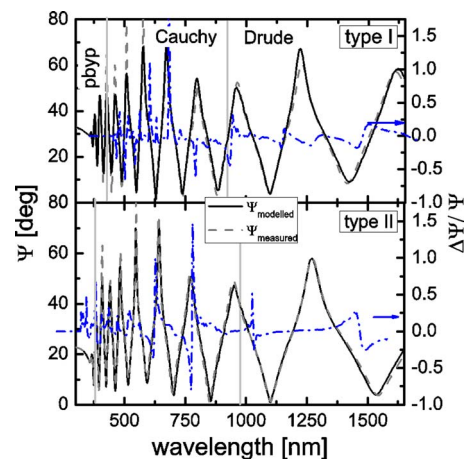


FIG. 4. (Color online) The ellipsometric parameter  $\Psi$  for a 940 nm-rough (type I) and 820 nm-smooth (type II) AZO film. The quality of the fit is expressed by the comparison between the measured and the modeled  $\Psi$  values and by the relative residue  $\Delta\Psi/\Psi$ . (Note: “pbyp” designates the point by point fit.)

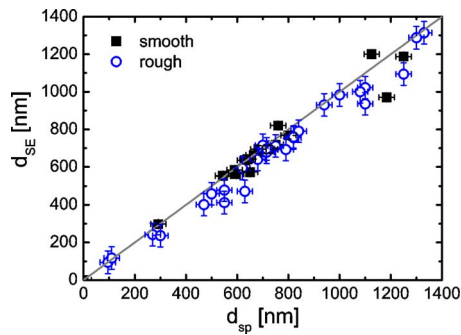


FIG. 5. (Color online) The film thickness of several smooth ( $\square$ ) and rough ( $\circ$ ) AZO films, as determined from ellipsometry ( $d_{SE}=d_b+d_r$ ) and step profiler ( $d_{sp}$ ).

( $10^{18} \text{ cm}^{-3}$ ), resulting in a high transmission for the whole measured wavelength range. With increasing conductivity (from type II to type I), a clear deviation of the Cauchy model from the point by point curve is visible at 900–1000 nm. This can also be used as an onset wavelength for the application of the Drude model. The optical constants shown in Fig. 6 are in agreement with the values reported in the literature.<sup>44,45</sup> The comparison with the literature should be, however, regarded with some reserve because the optical constants depend strongly on the doping level, as seen also in Table III, and possibly on other factors, such as thickness, stoichiometry, or crystallinity. Ideally, the comparison should be made with films having similar properties, which is quite difficult to achieve because of the incomplete information found in most of the ellipsometry studies on ZnO.

The doping is known to decrease the refractive index of the ZnO films<sup>46</sup> and this can also be observed in our case in Fig. 6. When performing a point by point fit in region A for the undoped and the AZO films, a blueshift in the position of the band gap absorption peak is observed. The increase in the ZnO band gap energy with doping is generally attributed to the Burstein–Moss shift,<sup>47</sup> caused by the filling of the lower states of the conduction band at high electron concentrations, as also reported in our earlier work.<sup>26</sup>

The Drude parameters are directly related to the electron conduction in the material and are listed in Table III. Again, it was difficult to find Drude parameter values reported for

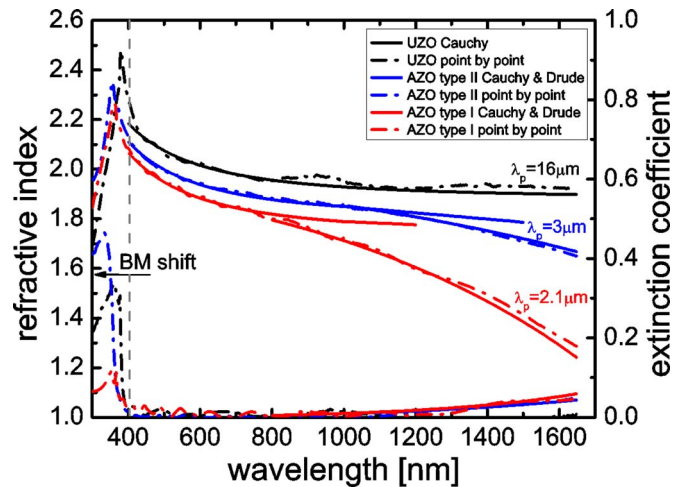


FIG. 6. (Color online) The optical constants of the AZO films determined from Cauchy (400–1000 nm) and Drude (1000–1700 nm) models; the comparison with the UZO films and with the point by point fit (300–1700 nm) is also shown.

similar ZnO films. In order to make a rough comparison, we chose to mention for the references in Table III also the film thickness and electron concentration, when possible. The onset of the free carrier absorption is given by the plasma wavelength, which can be calculated for the ZnO films according to the formula<sup>48</sup>

$$\lambda_p = 2\pi c \left( \frac{m_e^* \epsilon_\infty \epsilon_0}{e^2 N_e} \right)^{1/2}. \quad (8)$$

The plasma wavelength values calculated with Eq. (8) for the types I and II films are 2.1 and 3  $\mu\text{m}$ , respectively. The difference in plasma wavelength between the two types of films is given by the electron concentration but also by the refractive index/high energy dielectric constant  $\epsilon_\infty$  (cf. Table III). A shorter plasma wavelength for the type II films implies a lower transmission in region C (Fig. 3). The decrease in plasma wavelength causes also a steeper decrease in the refractive index trend (Fig. 6). The extinction coefficient of the AZO films increases in region C in comparison to the undoped sample. On the other hand, its values for types I and II AZO samples are comparable, due to similar  $\lambda_p$  and to the

TABLE III. Cauchy–Drude parameters and comparison with the literature.

	ZnO:Al type I	ZnO:Al type II	ZnO:Al/ZnO:Ga <sup>a</sup>	ZnO:Ga <sup>b</sup>	ZnO:Ga <sup>b</sup>
Cauchy					
A	1.74	1.8	...	...	...
B	0.053	0.05	...	...	...
$n$ @633 nm	1.86	1.92	1.83–1.87	1.75	1.85
Drude					
$\epsilon$ ( $\infty$ )	3.8	3.9	Not reported	3.65–3.9	...
$A_D$ (eV)	1.29	0.66	1.3/1.2	2.54	...
$\Gamma_D$ (eV)	0.04	0.1	0.17/0.11	0.13	...
$\lambda_p$ ( $\mu\text{m}$ )	2.1	3	Not reported	1.48	...
$d_{sp}$ (nm)	<b>940</b>	<b>820</b>	485/155	65	65
$N_e$ ( $\text{cm}^{-3}$ )	$2 \times 10^{20}$	$1 \times 10^{20}$	Not reported	$6.5 \times 10^{20}$	$4.8 \times 10^{20}$

<sup>a</sup>See Ref. 46.

<sup>b</sup>See Ref. 14.

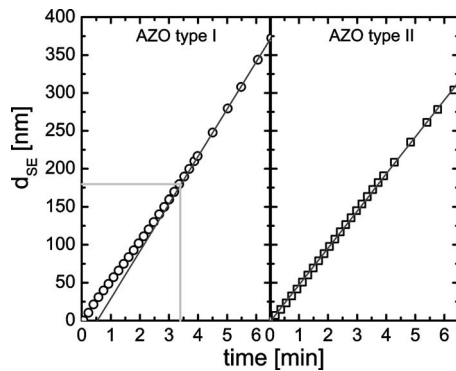


FIG. 7. The type I (pyramidlike) and type II (pillarlike) AZO film thickness evolution during growth; the time interval between the data was increased for the bulk growth region for clarity; only the first part of the bulk growth region is shown.

fact that  $\lambda < \lambda_p$  in the whole ellipsometry wavelength range.

To conclude, via comparisons with *ex situ* and literature data, we have demonstrated in this section that the Cauchy–Drude model is a good representation for the AZO films presented in this study. Therefore, in the next part we will address the results on the film growth and electronic properties derived from this model, applied to both *ex situ* and *in situ* SE data.

### III. RESULTS AND DISCUSSION

As already mentioned in Sec. I, this article continues the work presented in Ref. 11 and introduces the *in situ* and real time SE studies of the pyramidlike (type I) and pillarlike (type II) AZO films grown by means of remote PE-MOCVD.

#### A. *In situ* real time ZnO film growth studies

##### 1. Thickness evolution

The bulk and roughness layer thickness values,  $d_b$  and  $d_r$ , are the parameters fitted from the real time data at each time step. In Fig. 7 the total film thickness,  $d = d_b + d_r/2$ , as determined from the Cauchy model, is shown as a function of the deposition time, for both types I and II AZO films. A linear thickness development can be observed for all AZO samples and the bulk deposition rate, as calculated from the slope of the thickness curve, is higher for the type I films, i.e., 1 nm/s compared to 0.7 nm/s for type II films. This can be due to a higher growth flux arriving at the substrate under these conditions, caused by a factor of 4 higher pressure.

Besides the difference in deposition rate, a distinctive growth behavior in the first 150–200 nm can be observed, while for the type II films the deposition rate is constant in time already from the initial stages of deposition, a clear slower growth rate is present in the initial phase of the growth for type I samples; this is reproducible for a significant number of films under these growth conditions. The earlier TOF-SIMS measurements [Fig. 1(a)] indicated an initial incubation layer of about 150 nm for type I and less than 20 nm for type II films. When modeling the real time SE data, the refractive index is assumed to be constant at the bulk value, which means that the information on the incubation layer is included entirely in the thickness trend. Never-

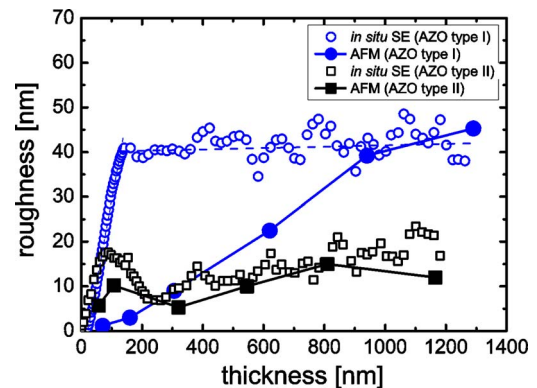


FIG. 8. (Color online) The evolution of the film roughness during type I (pyramidlike) and type II (pillarlike) AZO film growth from SE and AFM analyses.

theless, the SIMS and ellipsometric outcomes, i.e., the thickness of the incubation layer and the slower initial growth, respectively, agree, pointing out that less ZnO is deposited in the beginning of the growth for the type I AZO samples, caused either by an effective slower growth or by a higher porosity.<sup>49</sup> The difference in the growth process observed for the two types of films can, therefore, be attributed to a difference in plasma chemistry (growth species and flux) but also in surface mobility, as discussed in more detail in our previous article.<sup>11</sup>

##### 2. Roughness evolution

In our deposition system both very rough as well as relatively smooth films can be deposited (Table I).<sup>11</sup> For the smoother (type II) films, with columnar structure, the agreement between the SE and AFM outcomes is fairly good, as it can be observed in Fig. 8. For the rough (type I) samples, on the other hand, the roughness development differs significantly between the two techniques. SE shows a strong increase in roughness in the first 200 nm, corresponding to the initial growth, followed by a plateau, while, according to the AFM measurements, the roughness develops linearly up to 1  $\mu\text{m}$  film thickness (Fig. 8).<sup>50</sup> The difference in the values obtained by the two techniques can be rationalized if we consider the distinctive nature of the SE and AFM roughness measurements: SE roughness is a mixture of material and voids ( $d_r$ ), while AFM “physically” measures the average height of the features on top of the film bulk [root-mean-square (rms)]. The exact relationship between them is not known, being still under debate.<sup>51–53</sup> Nevertheless, the roughness evolution with thickness, as measured with SE and AFM, should be comparable if the roughness features develop in one (growth) direction. This is confirmed in the case of type II AZO films, with a pillarlike structure, where the void and height trends coincide due to the preferential grain evolution along film growth direction [Fig. 1(b)]. The pyramidlike grains present in the type I films, on the other hand, develop both in height and width [Fig. 1(b)]. As a result, although the rms increases, the lateral grain development leads to a decrease of the void fraction, resulting, by compensation with the height, in a constant roughness layer thickness determined by SE. Note that the optical model



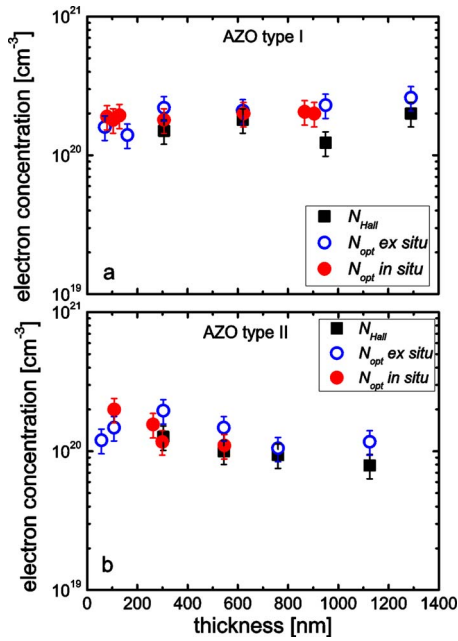


FIG. 9. (Color online) Comparison between the optical resistivity, as determined from *ex situ* and *in situ* SE ( $\rho_{\text{opt}}$ ), and the electrical resistivity, determined from four point probe, both as-measured ( $\rho_{\text{eff}}$ ) and corrected ( $\rho$ ) for (a) type I (pyramidlike) and (b) type II (pillarlike) AZO films.

used here assumes a constant void fraction of 50%, which can be physically incorrect. Nevertheless, introducing a void fraction gradient in the model is not useful due to the high correlation with the other parameters. Therefore, the roughness layer evolution should be seen as a combination of the height and voids development.

In conclusion, we have demonstrated that SE can be used *in situ* and real time for ZnO and provides key insights into the structural properties of the growing film. The use of a simple Cauchy model allows identifying and predicting the two growth modes, pyramidlike and pillarlike, from the thickness development in the initial growth phase and from the roughness evolution during the bulk growth.

## B. Electronic properties of the AZO films

### 1. Resistivity evolution

Besides the growth studies, the SE measurements can also be used to provide information about the electronic properties of the AZO films. The carrier concentration, resistivity, and mobility can be determined from the Drude parameters ( $\varepsilon_{\infty}, A_D, \Gamma_D$ ), according to Eqs. (6a)–(6c), mentioned in Sec. II B. The electronic parameters determined in this way give information about the in grain properties of the AZO films, since the electrons, when oscillating in an alternating current field at optical frequencies, have an amplitude which is much smaller than the grain size.

In Ref. 11 we defined the effective resistivity as  $R_s d$ , obtained from four point probe ( $R_s$ ) and step profiler measurements ( $d$ ). In Fig. 9, the SE resistivity values  $\rho_{\text{opt}}(d)$ , determined from Eq. (6a) for both types I and II AZO films, are compared with the effective resistivity values. Note that the resistivity, as determined from SE, is independent of the

choice of the electron effective mass, the main cause for errors in this optical analysis, for both types of AZO films.

In the case of type II films,  $\rho_{\text{opt}}(d)$  values are lower than  $R_s d(d)$  in the whole thickness range, indicating that the electron transport is limited by the carrier scattering at grain boundaries. For type I films, on the other hand, the difference between the SE and electrical resistivity values reduces with increasing thickness, which is in agreement with the outcomes related to grain development determined by SEM and AFM and with the initial porosity discussed in Ref. 11. However, despite the well-developed grains for film thicknesses larger than 1  $\mu\text{m}$ , the resistivities obtained from SE are always below the values determined from the electrical measurements (cf. Fig. 9). This difference can be misleading and, in order to explain it, we need to take into account the fact that the effective resistivity  $R_s d$  represents an integrated value over the film thickness  $d$ , being affected by the layers below, as previously reported<sup>11</sup>

$$\frac{d}{\rho_{\text{eff}}(d)} = \frac{1}{R_s(d)} = \int_0^d \frac{1}{\rho(x)} dx, \quad (9)$$

where  $\rho(x)$  represents the resistivity of the top layer of a deposited film with thickness  $x$ . This calculation has been presented in detail in Ref. 11. Since the observed sheet resistance  $R_s(d)$  scales with the film thickness, in the considered film thickness range, as

$$R_s(d) \sim d^{-(a+1)}. \quad (10)$$

The effective resistivity based on Eq. (9) can be determined to be

$$\rho(d) = \frac{\rho_{\text{eff}}(d)}{a+1} = \frac{R_s(d)d}{a+1}. \quad (11)$$

For type I films we found  $a = 2.2 \pm 0.5$ . For type II films this correction in  $\rho_{\text{eff}}(d)$  is not necessary due to the absence of gradient and, implicitly, of the thickness influence on resistivity.

Since the SE results reflect the in grain electrical properties of the material, the comparison with the corrected, local values  $\rho(d)$  gives a better estimation of the grain boundary influence on the electron conduction, especially for the thick type I films because  $\rho(d)$  reflects the top grain size, which is the largest at thickness  $d$ . Above film thickness values of  $\sim 1 \mu\text{m}$ , a good agreement is observed between the two techniques if we use the local  $\rho(d)$  values instead of  $\rho_{\text{eff}}(d)$ . This strongly suggests that, for thick films, the grain boundary effects are negligible and a further improvement of the resistivity should only be related to the intrinsic properties, i.e., doping level, impurities, etc.

Another interesting issue generates from the comparison between the *in situ* and the *ex situ* SE measurements performed during the growth of a thick ZnO film and on a thickness series corresponding to the same deposition conditions, respectively. The *ex situ* resistivity values in the case of type I are higher than the *in situ* values for films thinner than 300 nm [Fig. 9(a)]. This difference can be attributed to aging of these films, known to be porous (the *ex situ* measurements were performed a few months after the *in situ*

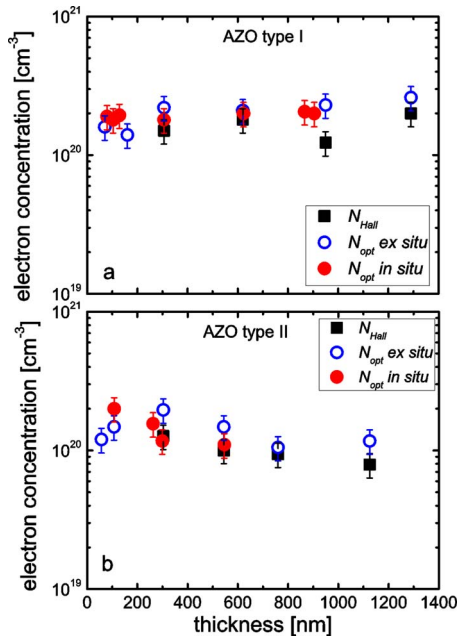


FIG. 10. (Color online) Comparison between the electron concentration determined by SE ( $N_{opt}$ ) and Hall ( $N_{Hall}$ ) measurements for (a) type I (pyramidlike) and (b) type II (pillarlike) AZO films. [Note: the very thin films ( $\leq 300$  nm) could not be measured with the Hall setup.]

ones). The film porosity normally leads to water uptake when exposed to atmosphere, influencing the optical constants of the film in the visible region (increase in refractive index<sup>54</sup>), but could also lead to a change in the Drude parameters in the near infrared region. The film aging detected by the Drude modeling, however, can imply that part of the aging occurs within the grain, i.e., the AZO matrix oxidizes and therefore the oxygen trap density increases.

## 2. Electron concentration and mobility

The SE electron concentration and mobility were calculated according to Eqs. (6b) and (6c) from Sec. II B and compared with the Hall measurements. The electron concentration  $N_{opt}(d)$  is independent of the film thickness, indicating constant intrinsic quality of the material for both types of films (Fig. 10).<sup>55</sup> An electron effective mass value of  $0.28m_e$  was used.<sup>14,26</sup> The choice of this value is validated by the agreement shown by the electron concentration values determined from SE and Hall, shown in Fig. 10, under the assumption that all electrons contributing to conduction are inside the grains.<sup>14</sup>

The effective mobility  $\mu_{eff}(d)$ , determined from the Hall measurements, reflects the resistivity behavior with thickness: it is constant for the films with pillarlike structure [Fig. 11(b)] and shows a strong gradient for the films with pyramidlike structure [Fig. 11(a)]. As shown in Fig. 11(a), the SE mobility is much higher than the Hall mobility for type II films, indicating that the electron conduction is grain boundary limited. The same occurs for type I films for film thicknesses below  $1 \mu\text{m}$  [Fig. 11(b)]. Similar results have been obtained by other groups<sup>14,56</sup> and indicate that the electron conductivity in these films is mainly limited by grain boundary scattering. This limitation is reduced during the growth

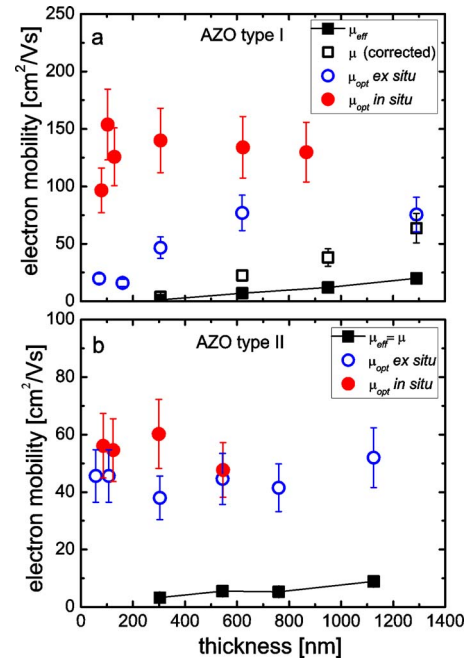


FIG. 11. (Color online) Comparison between the electron mobility determined by SE ( $\mu_{opt}$ ) and Hall, both as-measured ( $\mu_{eff}$ ) and corrected ( $\mu$ ) for (a) type I (pyramidlike) and (b) type II (pillarlike) AZO films. [Note: the very thin films ( $\leq 300$  nm) could not be measured with the Hall setup.]

of the films with pyramidlike structure, due to the grain development. For type I films thicker than  $1 \mu\text{m}$ , the difference between the two values is still visible, despite the well-developed grains. Similar to the observation on resistivity, this difference can be explained by the fact that the effective mobility is an integrated value over the film thickness. As a result, the values for thick films are reduced under the influence of the underneath layers. The corrected values of the electrical mobility, following a similar calculation as for the resistivity of type I films, are given by the relation

$$\mu(d) = (a + 1)\mu_{eff}(d), \quad (12)$$

with  $a = 2.2 \pm 0.5$ , which, as seen in Fig. 11, lead to similar values to the SE mobility, for films thicker than  $1 \mu\text{m}$ , showing that, in this case, the electron conduction is limited by the intrinsic properties of the material. For type II films this correction is not necessary, due to the relatively constant grain development.

The lower SE mobility for type II films, i.e.,  $\sim 50 \text{ cm}^2/\text{V s}$  compared with excellent values of  $\sim 100 \text{ cm}^2/\text{V s}$  for type I, suggests that the impurity content of the grains is higher in the first case.<sup>57</sup>  $\text{AlO}_x$  islands are commonly believed to be formed in the AZO films<sup>36</sup> although very few studies on the forms of Al incorporation have been reported so far.<sup>58</sup> In our case, type II films contain higher amounts of Al than type I (Table I). About 80% of the Al incorporated in type II films is electrically inactive, compared to only 4% in the case of type I films.<sup>11</sup> The inactive Al could be generated from  $\text{AlO}_x$  islands embedded in the ZnO matrix. If we correlate this with the lower in grain mobilities in the case of type II films, we can speculate that  $\text{AlO}_x$  might



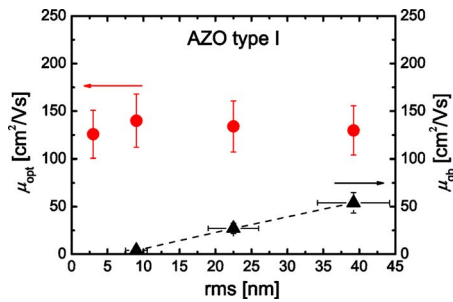


FIG. 12. (Color online) The in grain mobility ( $\mu_{\text{opt}}$ ) and grain boundary mobility ( $\mu_{\text{gb}}$ ) as a function of the rms values (a measure for the grain size) for type I (pyramidlike) AZO films. [Note: the very thin films ( $\leq 300$  nm) could not be measured with the Hall setup.]

incorporate within the grains, while other impurities, such as C or H, present in both types of films, could be segregated mainly at grain boundaries.

Again, similar to resistivity, the comparison between *in situ* and *ex situ* SE results point out the decrease of the mobility determined by ellipsometry when the films are exposed to the atmosphere for a long time, due to aging effects. This observation is not valid for the pillarlike films, which are denser and, therefore, less sensitive to air exposure.

In order to distinguish between the impurity and grain boundary scattering effects, Mathiessen's rule<sup>59</sup> can be applied, to a good approximation,<sup>60</sup> for the polycrystalline ZnO films

$$\frac{1}{\mu} = \frac{1}{\mu_i} + \frac{1}{\mu_{\text{gb}}}, \quad (13)$$

where  $\mu_i = \mu_{\text{opt}}$  accounts for the scattering mechanisms taking place in the grains (intrinsic mobility), while  $\mu_{\text{gb}}$  accounts for the effect of the grain boundaries on the electron mobility.

In Fig. 12 the ( $\leq 300$  nm) and ( $N_{\text{Hall}}$ ) are plotted as a function of the rms roughness values resulted from the AFM measurements (used here as a measure for the grain size). The  $\Delta\Psi/\Psi$  is practically independent of the grain size, while  $\mu_{\text{gb}}$  scales with it, in the case of type I films. This confirms the fact that the intrinsic properties of the material are constant and gives an indication of the grain size influence on the electron mobility. In the case of type II films, we chose not to show the dependence of the mobility of the grain size because the rms values are relatively constant (see Fig. 8) in the thickness range of the measured films, i.e., larger than 300 nm. More precise lateral grain size measurements, which could account for the small grain development, are necessary for these films.

#### IV. CONCLUSIONS

In this work *in situ* and real time VIS-NIR spectroscopic ellipsometry was applied to monitor and discern the growth modes of the Al-doped ZnO films deposited by remote PE-MOCVD. After a careful comparison between the optical analysis, the outcome of other *ex situ* diagnostic tools and literature studies on ZnO, it can be concluded that the Cauchy-Drude is an appropriate optical model to describe

the optical properties of ZnO in the studied wavelength range.

The identification of the growth mode could be performed real time by monitoring the thickness development in the initial growth stage and the roughness evolution during film growth. By applying a simple Cauchy model in the visible wavelength region differences between the pyramidlike (type I) and pillarlike (type II) AZO films could be identified: a slower growth rate was observed for the pyramidlike films during the initial phase compared to the bulk, while the pillarlike films exhibited a linear increase in thickness at all stages of growth. A saturation behavior in the roughness evolution for films thicker than 150–200 nm was observed for the pyramidlike structure, while for pillarlike films the roughness scales linearly with the film thickness. The relation between these differences and the two growth modes was validated by comparison with *ex situ* measurements, such as TOF-SIMS (initial growth) and AFM (roughness).

In the near infrared region, where free carrier absorption is present, spectroscopic ellipsometry was employed to probe the in grain electronic properties of the material. The results obtained from the Drude model demonstrate excellent in grain mobility values, i.e., above 100 cm<sup>2</sup>/V s (type I) and 50 cm<sup>2</sup>/V s (type II), independent of the film thickness. These values are much higher than the ones provided by the Hall measurements, which indicates that the limiting factor for the electron transport in these films is the scattering at grain boundaries.

Summarizing, the results presented in this article illustrate that spectroscopic ellipsometry is a useful tool for real time monitoring and predicting the growth mode of Al-doped ZnO films. Moreover, the SE studies in the near infrared region suggest that an increase in the grain size, leading to a decrease in the number of grain boundaries could lead to further improvement of the electrical properties of our material, especially in the case of the pillarlike films. The lower in grain mobility values exhibited by the type II layers show that there is also room for improvement in the intrinsic properties of the material (impurities, doping level, etc.). For the pyramidlike films, on the other hand, good electrical mobility values, close to the optical ones, are reached at the top of the film for film thickness above 1  $\mu\text{m}$ , due to the well-developed grains. For these films, further studies should be focused mainly on increasing the grain size at initial stages of growth in order to limit the gradient development and, thus, improve the sheet resistance.

#### ACKNOWLEDGMENTS

The authors wish to thank M. J. F. van de Sande, J. F. C. Jansen, J. J. A. Zeebregts (all of TU/e), and G. Kirchner (TNO) for their technical assistance. This work was supported by the Netherlands Organization for Applied Scientific Research (TNO) and the Eindhoven University of Technology (TU/e) through the program for Sustainable Energy Technology.

<sup>1</sup>R. Groenen, J. Löffler, J. L. Linden, R. E. I. Schropp, and M. C. M. van de Sanden, *Thin Solid Films* **492**, 298 (2005).

<sup>2</sup>M. Berginski, J. Hupkes, M. Schulte, G. Schope, H. Stiebig, B. Rech, and

- M. Wuttig, J. Appl. Phys. **101**, 074903 (2007).
- <sup>3</sup>T. Minami, Semicond. Sci. Technol. **20**, S35 (2005).
  - <sup>4</sup>O. Kluth, G. Schope, B. Rech, R. Menner, M. Oertel, K. Orgassa, and H. W. Schock, Thin Solid Films **502**, 311 (2006).
  - <sup>5</sup>M. Dinescu and P. Verardi, Appl. Surf. Sci. **106**, 149 (1996).
  - <sup>6</sup>J. H. Hu and R. G. Gordon, Sol. Cells **30**, 437 (1991).
  - <sup>7</sup>S. Fay, U. Kroll, C. Bucher, E. Vallat-Sauvain, and A. Shah, Sol. Energy Mater. Sol. Cells **86**, 385 (2005).
  - <sup>8</sup>J. J. Robbins, J. Harvey, J. Leaf, C. Fry, and C. A. Wolden, Thin Solid Films **473**, 35 (2005).
  - <sup>9</sup>R. Groenen, J. Löffler, P. M. Sommeling, J. L. Linden, E. A. G. Hamers, R. E. I. Schropp, and M. C. M. van de Sanden, Thin Solid Films **392**, 226 (2001).
  - <sup>10</sup>S. Fay, L. Feitknecht, R. Schluchter, U. Kroll, E. Vallat-Sauvain, and A. Shah, Sol. Energy Mater. Sol. Cells **90**, 2960 (2006).
  - <sup>11</sup>I. Volintiru, M. Creatore, B. J. Kniknie, C. I. M. A. Spee, and M. C. M. van de Sanden, J. Appl. Phys. **102**, 043709 (2007).
  - <sup>12</sup>The sheet resistance of all films was measured immediately after deposition, while the Hall measurements were performed a few months later.
  - <sup>13</sup>M. Creatore, M. Kilic, K. O'Brien, R. Groenen, and M. C. M. van de Sanden, Thin Solid Films **427**, 137 (2003).
  - <sup>14</sup>H. Fujiwara and M. Kondo, Phys. Rev. B **71**, 075109 (2005).
  - <sup>15</sup>R. A. Synowicki, Thin Solid Films **313–314**, 394 (1998).
  - <sup>16</sup>W. M. M. Kessels, J. P. M. Hoefnagels, E. Langereis, and M. C. M. van de Sanden, Thin Solid Films **501**, 88 (2006).
  - <sup>17</sup>R. W. Collins, A. S. Ferlauto, G. M. Ferreira, C. Chen, J. Koh, R. J. Koval, Y. Lee, J. M. Pearce, and C. R. Wronski, Sol. Energy Mater. Sol. Cells **78**, 143 (2003).
  - <sup>18</sup>T. W. H. Oates, D. R. McKenzie, and M. M. M. Bilek, Phys. Rev. B **70**, 195406 (2004).
  - <sup>19</sup>A. Amassian, P. Desjardins, and L. Martinu, Thin Solid Films **447–448**, 40 (2004).
  - <sup>20</sup>G. Bruno, M. Losurdo, M. M. Giangregorio, P. Capezzuto, A. S. Brown, T. H. Kim, and S. Choi, Appl. Surf. Sci. **253**, 219 (2006).
  - <sup>21</sup>M. Losurdo, M. M. Giangregorio, P. Capezzuto, G. Bruno, G. Malandrino, A. Blandino, and I. L. Fragala, Superlattices Microstruct. **38**, 291 (2005).
  - <sup>22</sup>R. Groenen, M. Creatore, and M. C. M. van de Sanden, Appl. Surf. Sci. **241**, 321 (2005).
  - <sup>23</sup>I. Volintiru, M. Creatore, J. L. Linden, and M. C. M. van de Sanden, Superlattices Microstruct. **39**, 348 (2006).
  - <sup>24</sup>D. Sainju, P. J. v. d. Oever, N. J. Podraza, M. Syed, J. A. Stoke, J. Chen, X. Yang, X. Deng, and R. W. Collins, Proceedings of IEEE 4th World Conference on Photovoltaic Energy Conversion, 2006, p. 475 (unpublished).
  - <sup>25</sup>M. C. M. Van de Sanden, J. M. de Regt, and D. C. Schram, Plasma Sources Sci. Technol. **3**, 501 (1994).
  - <sup>26</sup>R. Groenen, E. R. Kieft, J. L. Linden, and M. C. M. Van de Sanden, J. Electron. Mater. **35**, 711 (2006).
  - <sup>27</sup>H. El Rhaleb, E. Benamar, M. Rami, J. P. Roger, A. Hakam, and A. Ennaoui, Appl. Surf. Sci. **201**, 138 (2002).
  - <sup>28</sup>G. E. Jellison and L. A. Boatner, Phys. Rev. B **58**, 3586 (1998).
  - <sup>29</sup>M. Losurdo, Thin Solid Films **455–456**, 301 (2004).
  - <sup>30</sup>L.-J. Meng, E. Crossan, A. Voronov, and F. Placido, Thin Solid Films **422**, 80 (2002).
  - <sup>31</sup>Y. S. Jung, Thin Solid Films **467**, 36 (2004).
  - <sup>32</sup>Y. C. Liu, S. K. Tung, and J. H. Hsieh, J. Cryst. Growth **287**, 105 (2006).
  - <sup>33</sup>Z. F. Liu, F. K. Shan, Y. X. Li, B. C. Shin, and Y. S. Yu, J. Cryst. Growth **259**, 130 (2003).
  - <sup>34</sup>H. Fujiwara, *Spectroscopic Ellipsometry, Principles and Applications* (Wiley, New York, 2007).
  - <sup>35</sup>K. Zhang, A. R. Forouhi, and I. Bloomer, J. Vac. Sci. Technol. A **17**, 1843 (1999).
  - <sup>36</sup>S. Brehme, F. Fenske, W. Fuhs, E. Nebauer, M. Poschenrieder, B. Selle, and I. Sieber, Thin Solid Films **342**, 167 (1999).
  - <sup>37</sup>E. Langereis, S. B. S. Heil, M. C. M. van de Sanden, and W. M. M. Kessels, J. Appl. Phys. **100**, 023534 (2006).
  - <sup>38</sup>In the Drude free electron theory the  $\epsilon_\infty$  factor is not present in these formulas (like for metallike films). However, this factor is commonly used in the Drude modeling of TCOs, although reports in literature on its origin could not be found. We think that  $\epsilon_\infty$  accounts for the fact that the Drude model is applied within a limited range in the case of TCOs (sometimes below the plasma wavelength), which means that also contributions from the bounded electrons have to be taken into account (represented by  $\epsilon_\infty$ ).
  - <sup>39</sup>C. F. Bohren and D. R. Huffman, *Absorption and Scattering of Light by Small Particles* (Wiley-Interscience, New York, 1983).
  - <sup>40</sup>D. E. Aspnes and J. B. Theeten, Phys. Rev. B **20**, 3292 (1979).
  - <sup>41</sup>P. I. Rovira and R. W. Collins, J. Appl. Phys. **85**, 2015 (1999).
  - <sup>42</sup>The total SE thickness of the films, proportional with the amount of material deposited, is given by the relation:  $d = d_b + d_r/2$  (see Sec. III B 1); this results from the definition of the surface layer roughness (50% material and 50% voids). In order to be able to compare with the step profiler thickness  $d_{sp}$ , however, this relation needs to be adjusted because the step profiler measures the difference top-bottom of the film, therefore probing the sum of the bulk and roughness layer thickness  $d_b + d_r$ .
  - <sup>43</sup>In the point by point fitting procedure the same model as for the Cauchy/Drude models was used. Only the refractive index was fitted, while keeping the thickness of the bulk and roughness layer constant. The oscillations observed in both refractive index and extinction coefficient could be an artifact of the simplified model, i.e., the fixed thickness values.
  - <sup>44</sup>Y. Yang, X. W. Sun, B. J. Chen, C. X. Xu, T. P. Chen, C. Q. Sun, B. K. Tay, and Z. Sun, Thin Solid Films **510**, 95 (2006).
  - <sup>45</sup>Y. Qu, T. A. Gessert, K. Ramanathan, R. G. Dhere, R. Noufi, and T. J. Coutts, J. Vac. Sci. Technol. A **11**, 996 (1993).
  - <sup>46</sup>K. Postava, H. Sueki, M. Aoyama, T. Yamaguchi, K. Murakami, and Y. Igasaki, Appl. Surf. Sci. **175–176**, 543 (2001).
  - <sup>47</sup>E. Burstein, Phys. Rev. **93**, 632 (1954).
  - <sup>48</sup>H. L. Hartnagel, A. L. Dawar, A. K. Jain, and C. Jagadish, *Semiconducting Transparent Thin Films*, 1st ed. (Institute of Physics, Bristol, 1995).
  - <sup>49</sup>The deposition of ZnO films consists of two steps: first the growth species deposit on the Si substrate and then on the underlying ZnO layer. It is plausible to assume that the sticking coefficient is higher for the deposition on ZnO. Therefore, for type I films the growth species have to deposit on the Si substrate for longer time than for type II because of the poor ZnO nucleation.
  - <sup>50</sup>The small fluctuations in the optical surface roughness evolution are presumably caused by the interference occurring in the ZnO layer and leading to very low intensity of the signal reaching the detector for specific film thickness values [P. J. van den Oever, M. C. M. van de Sanden, and W. M. M. Kessels, Mater. Res. Soc. Symp. Proc. **808**, A9.35.1 (2004)].
  - <sup>51</sup>H. Fujiwara, M. Kondo, and A. Matsuda, Phys. Rev. B **63**, 115306 (2001).
  - <sup>52</sup>J. Koh, Y. W. Lu, C. R. Wronski, Y. L. Kuang, R. W. Collins, T. T. Tsong, and Y. E. Strausser, Appl. Phys. Lett. **69**, 1297 (1996).
  - <sup>53</sup>D. Franta, I. Ohlidal, P. Klapetek, and P. Pokorny, Surf. Interface Anal. **34**, 759 (2002).
  - <sup>54</sup>M. Creatore, J. C. Cigal, G. M. W. Kroesen, and M. C. M. van de Sanden, Thin Solid Films **484**, 104 (2005).
  - <sup>55</sup>The constant dopant level with the film thickness demonstrates that the films can be treated optically as a homogeneous medium, which simplifies the SE modeling, especially in the NIR region.
  - <sup>56</sup>J. Steinhäuser, S. Fay, N. Oliveira, E. Vallat-Sauvain, and C. Ballif, Appl. Phys. Lett. **90**, 142107 (2007).
  - <sup>57</sup>Groenen *et al.* calculated in their paper (Ref. 26) a factor of 3 lower SE mobilities than in this paper. We want to stress that, although his Al-doped ZnO films were deposited by the same technique, the deposition conditions and reactor geometry were different, which could cause worse intrinsic film quality.
  - <sup>58</sup>I. Sieber, N. Wanderka, I. Urban, I. Dorfel, E. Schierhorn, F. Fenske, and W. Fuhs, Thin Solid Films **330**, 108 (1998).
  - <sup>59</sup>C. Kittel, *Introduction to Solid State Physics* (Wiley, New York, 1996), p. 159.
  - <sup>60</sup>A. F. Mayadas and M. Shatzkes, Phys. Rev. B **1**, 1382 (1970).